




Template-Induced Graphitic Nanodomains in Nitrogen-Doped Carbons Enable High-Performance Sodium-Ion Capacitors

Chun Li* , Zihan Song, Minliang Liu, Enrico Lepre, Markus Antonietti, Junwu Zhu, Jian Liu , Yongsheng Fu*, and Nieves López-Salas* 

Sodium-ion capacitors (SICs) have great potential in energy storage due to their low cost, the abundance of Na, and the potential to deliver high energy and power simultaneously. This article demonstrates a template-assisted method to induce graphitic nanodomains and micro-mesopores into nitrogen-doped carbons. This study elucidates that these graphitic nanodomains are beneficial for Na⁺ storage. The obtained N-doped carbon (As8Mg) electrode achieved a reversible capacity of 254 mA h g⁻¹ at 0.1 A g⁻¹. Moreover, the As8Mg-based SIC device achieves high combinations of power/energy densities (53 W kg⁻¹ at 224 Wh kg⁻¹ and 10 410 W kg⁻¹ at 51 Wh kg⁻¹) with outstanding cycle stability (99.7% retention over 600 cycles at 0.2 A g⁻¹). Our findings provide insights into optimizing carbon's microstructure to boost sodium storage in the pseudocapacitive mode.

1. Introduction

Electrical energy storage systems (EES) play an essential role in portable instruments, electric mobility, data storage systems, aerospace, and stationary markets. Energy storage devices that exhibit high energy density, high-power density, and good cycle stability, such as rechargeable batteries and electrochemical supercapacitors (SCs), are drawing tremendous attention. However, there is a huge global need for EES that can provide simultaneous high energy density and high-power density. After lithium-ion batteries (LIB) were successfully commercialized in the 1990s, Amatucci et al. constructed the first lithium-ion capacitors

Dr. C. Li, M. Liu, Prof. J. Zhu, Prof. Y. Fu
Key Laboratory for Soft Chemistry and Functional Materials of Ministry of Education, Nanjing University of Science and Technology, Nanjing 210094, China

E-mail: chunli19950213@gmail.com


E-mail: fuyongsheng@njjust.edu.cn

Dr. C. Li, Dr. Z. Song, Dr. E. Lepre, Prof. M. Antonietti, Prof. N. López-Salas
Colloid Chemistry Department, Max Planck Institute of Colloids and Interfaces, Am Mühlenberg 1, 14476, Potsdam, Germany

E-mail: nieves.lopezsalas@mpikg.mpg.de

Prof. J. Liu

School of Engineering, Faculty of Applied Science, University of British Columbia, Kelowna, British Columbia V1V1V7, Canada

 The ORCID identification number(s) for the author(s) of this article can be found under <https://doi.org/10.1002/eam2.12695>.

DOI: 10.1002/eam2.12695

(LICs) using active carbon (AC) as cathode and Li₄Ti₅O₁₂ as anode, which exhibited three times larger energy density than that of traditional carbon-based SCs, and a high-power density at the same time.^[1] Despite the many successfully assembled devices, the concern about the cost and reserves of lithium, especially in smart grids and large-scale energy devices, stimulates the idea of expanding lithium with earth-abundant sodium that has similar properties to lithium. Even though, the larger size of sodium-ion (1.02 Å) than lithium-ion (0.76 Å) hinders high sodium storage capacity and fast ion diffusion, especially on the anodic side.^[2,3] Rapid development and increasing research into SICs have been seen in the past 10 years after Amatucci and his colleagues constructed sodium-ion capacitors (SICs) with hard carbon (HC) as

anodes and AC as cathodes in 2012. Excitingly, SICs deliver both high energy and power density simultaneously, showing the potential to cross the gap between traditional SCs and batteries.

In order to achieve high performance, hybrid cells constructed by high-rate cathodes and large capacity anodes, for instance, traditional electrical double-layer capacitor (EDLC) cathodes further assembled with battery-type anodes, are the main configurations explored in SICs devices. Furthermore, pseudocapacitive materials provide more cell configurations for SICs as they can replace capacitive and battery-type electrodes.^[4] These materials store charge through redox reactions like batteries but at fast rates comparable to EDLC, providing a pathway to achieve high energy and power densities.^[5,6] In supercapacitors, anodes and cathodes have to store both cations and anions, respectively, and even devices containing the same carbon material with different surface functional groups are asymmetric supercapacitors.^[7] Nevertheless, cell configurations involving high surface area carbon materials as both anode and cathode usually are not assigned to the SIC branding, where two electrodes with different charge storage mechanisms are paired. Even so, pure sodium-based capacitive energy storage devices have been reported to exhibit very high performance.^[8–10] For example, Ding et al. assembled a full cell capacitor with a N, O-doped porous carbon anode and a capacitive cathode, demonstrating an attractive energy density of 111 Wh kg⁻¹ and a high cycling stability.^[11] Thus, in this article, we consider the configuration of capacitive cathodes and pseudocapacitive anodes with same charge storage character as SICs.

A variety of pseudocapacitive materials have been investigated for the realization of fast-charging energy storage devices with long-lasting

high power, including carbons,^[12] oxides,^[13,14] nitrides,^[15] sulfides,^[16,17] and sodium fluorophosphates.^[18] Among them, microstructurally designed carbons might be the most economically and technically feasible candidates due to their low costs, low structural molecular weight, and long-term cycling performance.^[19] At present, hard carbons (HCs) with randomly distributed graphene layers and sub-nanometer slit pores between the covalent layers are the most promising anode materials, and deliver a reversible capacity in the range of 150–350 mAh g⁻¹ but often suffer from poor rate performance and cycling performance. The irreversible capacity loss of HCs is mainly caused by sodium-intercalation-expansion in HCs, which gradually damages the graphitized nanodomains in HCs and cause fast decay of plateau capacity.^[20,21] In comparison, soft carbons (SCs) with small graphitic domains and relatively fewer defects exhibited superior rate and cycling performance but relatively low capacity.^[22,23] Therefore, constructing a hybrid structure of tectonically arranged, nanosized graphitic structures is an inspiring approach to construct rational frameworks of carbonaceous materials for better SICs performance.

Apart from the intrinsic carbon framework, pore distribution and heteroatom doping are important factors for enhancing sodium storage and reversible capacity. Porous carbons (PCs) are widely explored in electrochemical capacitors. Gogotsi *et al.* demonstrated that electrolyte ions could enter sub-nanopores without their solvation shell, facilitating charge storage.^[24] Le *et al.* reported that mesopores in the porous heterostructure shorten the ionic pathway throughout the active material grains in the electrode.^[25] Hierarchical structures with a combination of macro-meso-micropores are considered to be beneficial for electrolyte penetration and accommodating volume expansion.^[26] In addition, heteroatom doping, especially nitrogen, has also been proven to be an effective way to enhance Na storage by providing accessible sites, inducing an extra pseudo-Faradic capacity^[27] and sometimes expanding the interlayer spacing.^[28] Until now, many methods have been explored to develop carbons with tunable microstructure and improved Na⁺ storage, such as chemical vapor deposition,^[29] the hydrothermal method,^[30] and electrospinning.^[31] On top, templates are easy to implement and can effectively control the pore-size distribution of PCs, construct diverse morphologies, and guide carbon frameworks' growth to adjust interlayer spacing.^[32]

Herein, based on the above considerations, we demonstrated template-assisted synthesis strategy for producing N-doped carbon materials with tunable graphitic nanodomains arrangements, which can be achieved by modifying the salt and thermal-treatment condition. A tubular nitrogen-doped porous carbon (NPCs), named As8Mg, with enlarged interlayer distance and micro-mesoporous structure, was fabricated by a facile template-assisted method using MgCl₂·6H₂O as both template and salt melt solvent. The obtained As8Mg shows graphitic nanodomains that lead to strong pseudocapacitive energy storage. As8Mg delivered an excellent reversible capacity of 254 mA h g⁻¹ at 0.1 A g⁻¹ and 107 mA h g⁻¹ within the ultrafast charge–discharge process at 5 A g⁻¹. Meanwhile, As8Mg also displayed excellent cycling stability with a capacity retention of 98.7% after 350 cycles at 0.2 A g⁻¹. Finally, by coupling the As8Mg anode and a commercial active carbon (AC) cathode, a SIC was assembled and exhibited a broad voltage window (0.5–4 V), high energy storage density of 224 Wh kg⁻¹ at 53 W kg⁻¹, and high-power density of 10 410 W kg⁻¹ at 51 Wh kg⁻¹. The SIC device also exhibited high capacity retention of 99.7% at 0.2 A g⁻¹ after 600 charge–discharge cycles. Our findings demonstrated that the presence of pseudo-graphitic nanodomains, which are abundant in As8Mg, is the

predominant contribution to improving the Na storage capacity with a promising rate capability. The exploration of the microstructure and outstanding electrochemical performance of As8Mg in this work offers further inspiration for structural design and optimization of carbonaceous materials for energy storage.

2. Results and Discussion

Nitrogen-doped porous carbons (NPC) were synthesized using different templating methods. As8Mg and As9Mg were obtained from ion thermal templating with MgCl₂·6H₂O template, while As8Ca and As9Ca were prepared using CaCl₂·2H₂O as a template. The synthesis of As8Mg and As9Mg is similar to the work of Pampel *et al.* on nitrogen-doped carbons derived from adenine and MgCl₂·6H₂O.^[33,34] They reported that adenine participates in the growth of the final structure of the products by bonding to the water molecules of MgCl₂·4H₂O which is formed because of the recrystallization of MgCl₂·4H₂O after MgCl₂·6H₂O losing 2 water molecules at 96 °C. Adenine is assembled on the surface of the solid–liquid phase of MgCl₂·4H₂O and liquid MgCl₂·6H₂O, restricting further decomposition of MgCl₂·4H₂O. Thus, rectangular tubular or tunnel-like structures are formed by condensation by a cooperative templating process from both the salt and precursor. CaCl₂·2H₂O also experiences a state of liquid when it melts at 175 °C, but later forms a solid monohydrate and anhydrous CaCl₂ due to dehydration. In this case, the difference is that CaCl₂·2H₂O provides a homogeneous environment for the initial crosslinking of adenosine attached to CaCl₂·2H₂O. A relatively high yield of 34 wt% indicates that further condensation occurs (Table S1, Supporting Information). The later-in-synthesis re-solidified CaCl₂ pushes away the still plastic organic phase, serves as a hard template and generates porous carbon with a partially ordered nanostructure (As8Ca and As9Ca) with the demixed nanocrystals forming pores.

The morphologies and microstructures were investigated by transmission electron microscopy (TEM) and scanning electron microscopy (SEM) and are remarkably different. As8Mg exhibits a large range, highly parallel tubular structure (Figure 1a and Figure S1a, Supporting Information) with a length of a few micrometers. In Figure 1b, the magnified TEM image of the structure of As8Mg is a combination of locally disordered domains and rather well-organized, short but well-stacked graphitic nanodomains that take random orientations to each other. The corresponding interlayer spacing in these nanodomains is measured to be 0.37 ± 0.01 nm (Figure S2a–c, Supporting Information), which is in principle large enough for interlayer-insertion of Na.^[3] In addition, the tubular mesopores could provide transport channels and allow the electrolyte to penetrate into the whole electrode.

In contrast, the CaCl₂·2H₂O template made the nanosheets highly mesoporous, with roundish mesopores and an average mesopore diameter of 10 nm. The walls between those mesopores are built from several graphitic carbon layers, as shown in Figure 1d,e. It is speculated that supramolecular eutectic complexes of CaCl₂·2H₂O and adenosine confine the final graphitization conversion to a thin layer around the surface of CaCl₂-crystallites. As shown in the enlarged TEM image and corresponding intensity line profiles of As8Ca (Figure 1f and Figure S2d–f, Supporting Information), the As8Ca structure displays less ordered structures connecting layered graphitic stacking structures with an extended interlayer distance of 0.39 ± 0.01 nm, which could be active in Na insertion.

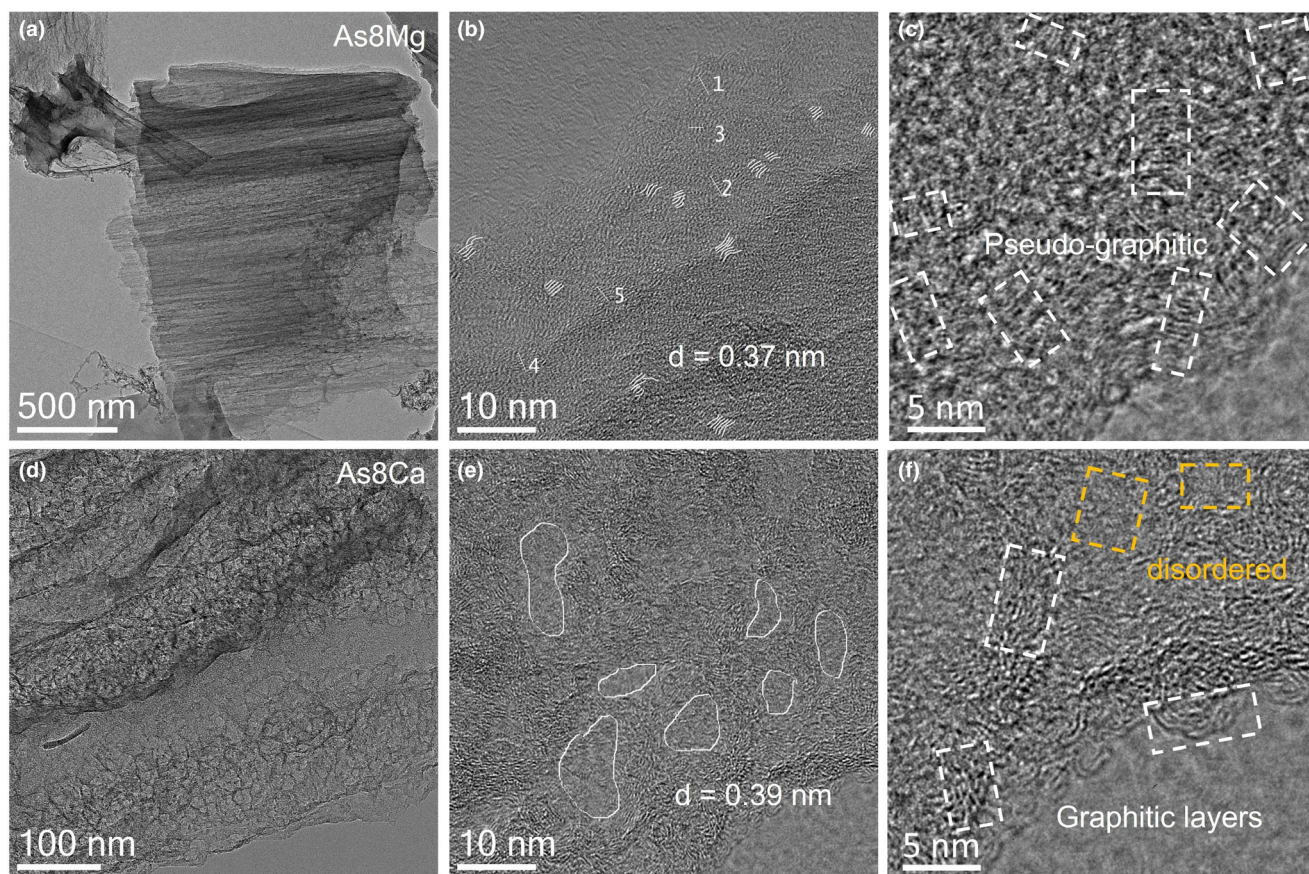


Figure 1. a, b) TEM image, c) HRTEM images of As8Mg, d, e) TEM image, f) HRTEM images of As8Ca.

When increasing the condensation temperature from 800 °C to 900 °C, the obtained NPCs maintain the tubular shape and nanosheet morphology, respectively, as shown in their SEM images (Figure S1, Supporting Information). However, the nanostructures differ. In the magnified TEM image of As9Mg (Figure S3b, Supporting Information), the graphitic nanodomains are missing, while the mesopores with layered walls found in As8Ca were still observed in As9Ca (Figure S3c,d, Supporting Information). We further pyrolyzed As8Mg and As8Ca at 900 °C for 2 h to generate samples As8Mg-9 and As8Ca-9 with yields of 60 and 70 wt%, respectively. The TEM images of As8Mg-9 and As8Ca-9 are shown in Figure S4, Supporting Information, both the graphitic nanodomains of As8Mg and the graphitic pore walls of As8Ca remained after 2 h of thermal condensation under 900 °C. The comparison of these 3 conditions makes it clear that, unlike $\text{CaCl}_2 \cdot 2\text{H}_2\text{O}$, a precondensation step at 800 °C is necessary to cross-link the carbonaceous framework in $\text{MgCl}_2 \cdot 6\text{H}_2\text{O}$ -templating system, while direct heating to higher temperatures does not result in the wanted structure, which may be caused by the etching effect from Mg species. The relatively lower yield of NPCs from $\text{MgCl}_2 \cdot 6\text{H}_2\text{O}$ -templating system also proved that the formation of the carbonaceous framework is less efficient than that of the $\text{CaCl}_2 \cdot 2\text{H}_2\text{O}$ system (Table S1, Supporting Information).

X-ray diffraction (XRD) and Raman spectroscopy were obtained to investigate the local organization of the four NPCs. The XRD patterns of the NPCs show very broad graphitic stacking peaks centered around

23–25°, which is due to the short-range order of the graphitic nanodomains. Meanwhile, in Figure S5, Supporting Information, the SEAD patterns of four NPCs showed diffused continuous and thick rings, confirming the lack of long-range ordered structure.^[35] The Raman spectra of the synthesized NPCs displayed two strong peaks at 1350 and 1582 cm^{-1} , which are classically assigned to the defects-containing carbon and sp^2 -hybridized carbon in aromatic structures, respectively (Figure 2b). The latter peak (1582 cm^{-1}) of As9Mg and As9Ca showed slightly smaller intensity than As8Mg and As8Ca, indicating the presence of a lower defect density, as more heteroatoms would be removed during higher-temperature pyrolysis. The specific surface area and pore structure were characterized via N_2 adsorption/desorption isotherms at 77 K (Figure 2c). All the NPCs demonstrated type-IV isotherms with hysteresis loops, suggesting the presence of micro- and mesopores in the pore network. The Brunauer–Emmett–Teller (BET) specific surface areas of As8Mg, As8Ca, As9Mg, and As9Ca were as large as 1466, 1358, 1445, and 887 $\text{m}^2 \text{g}^{-1}$, respectively, and the NPCs exhibit a high total pore volume (see Table S1, Supporting Information, for the values). As8Ca and As9Ca showed a narrower pore-size distribution centered at 10 nm (Figure 2d), which contributes most of the pore volume and could potentially serve as ion highways.^[36] Meanwhile, As8Mg and As9Mg showed more micropores, which could improve charge storage due to the confinement effect.^[37,38] We also have to underline that the enlarged stacking distance gives excessive potential sorption sites for Na, which are, however, clearly inaccessible for N_2 .

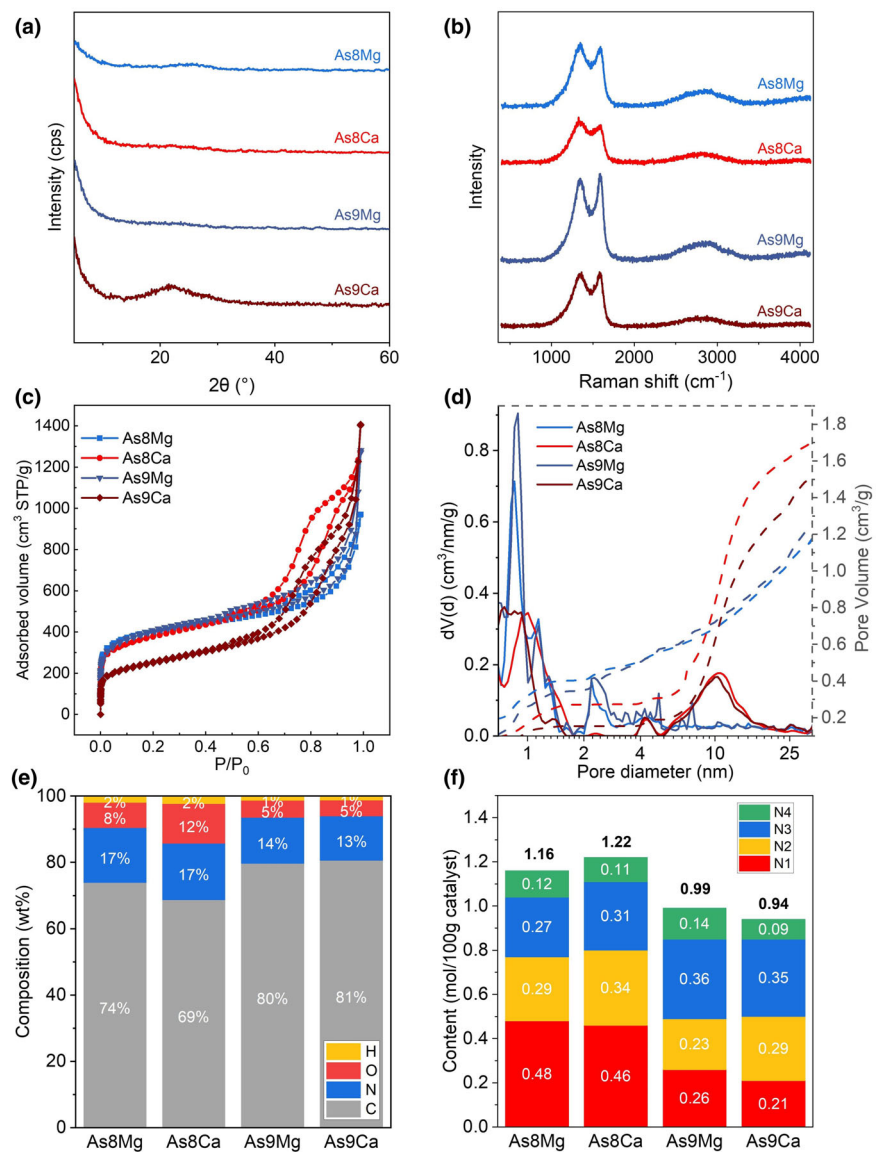


Figure 2. a) XRD patterns, b) Raman spectra, c) N_2 sorption isotherms, d) pore distribution, e) elemental composition, f) different N species content of As8Mg, As8Ca, As9Mg, and As9Ca.

The composition of the four NPCs was determined by elemental chemical analysis (EA in Table S2, Supporting Information) and X-ray photoelectron spectroscopy (XPS). The residue of Mg and Ca are less than 0.1 and 0.5 wt%, which is negligible in the performance of ion storage and other electrochemical properties. As8Mg and As8Ca have a high nitrogen content of 17% and decline to 13% and 14% for As9Mg and As9Ca from the EA results displayed in Figure 2e. The full scanning spectra of XPS (Figure S6a, Supporting Information) show three peaks of C, N, and O elements, and the corresponding elemental composition (Figure S6b, Supporting Information) shows lower heteroatoms content compared to the EA result, which might be caused by the limited detection depth and the resulting surface sensitivity of XPS. Thus, EA and XPS are to be combined to obtain more accurate content of different N species, the calculation is based on Equation 1:

$$C_N = w * a \quad (1)$$

Here, C_N is the mole of N species in 100 g catalysts, w is the weight percentage of N from EA results, and a is the atomic percentage of different N species obtained from N 1s XPS spectra (Figure S6c, Supporting Information) by deconvoluting the high-resolution spectra of N 1s into four peaks located at 398.4, 399.9, 401.2, and 403.7/402.3 eV, which are assigned to pyridinic N, pyrrolic N, quaternary N, and oxidized nitrogen functionalities, respectively (Figure 3). There is difference in peak position (green peak) between AsXMg (As8Mg and As9Mg) and AsXCa (As8Ca and As9Ca), indicating nitrogen in samples from $\text{CaCl}_2 \cdot \text{H}_2\text{O}$ is less oxidized than in samples from $\text{MgCl}_2 \cdot 6\text{H}_2\text{O}$, which is possibly due to different oxidized species resulting from the use of distinct salts and the etching effect from Mg species.

The C_N values are shown in Figure 2f. The loss of nitrogen by the 100 °C increase of pyrolysis temperature are 15% and 23% for $\text{MgCl}_2 \cdot 6\text{H}_2\text{O}$ and $\text{CaCl}_2 \cdot 2\text{H}_2\text{O}$ templating strategies, respectively, mainly on account of the pyridinic N. Bearing this in mind, the content and conjugation environment of nitrogen is essential for a high capacity and will be discussed in the electrochemical performance section.

The electrochemical performance of the NPCs electrodes was investigated via galvanostatic charge/discharge (GCD), cyclic voltammetry (CV), and electrochemical impedance spectroscopy (EIS) in half-cells. Figure 4a demonstrates the GCD curves of four NPCs electrodes at 0.2 A g^{-1} , which features only a sloping region without any obvious deposition plateau close to Na-standard potential. This implies a capacitive-dominated process in all four NPCs anodes based on their large surface area and rich defects, as displayed in all analytical data. CV curves also verify this surface-dominated mechanism with a nearly rectangular shape, shown in Figure 4b. The cathodic peak close to 0.01 V is ascribed to the intercalation of Na^+ into the graphitic domains and the reduction of Na^+ to Na^0 in structural voids.^[39] The oxidation current peak between 0.4–0.6 V should be ascribed to partly reversible sodium insertion into special positions next to residual H atoms in the carbon material.^[3,40] The rectangular shape of the CV curves with weak redox peaks also implies capacitive sodium storage behavior.

To investigate the rate performance of the NPCs electrodes, GCD tests were recorded under different current densities, as presented in Figure 4c. Overall, As8Mg delivers the highest capacity among four NPCs anodes, with capacities of 254, 208, 184, 159, 140, 107, 72, and 60 mAh g^{-1} at 0.1, 0.2, 0.5, 1, 2, 5, 10, and 20 A g^{-1} , respectively. Besides, when the current density returns to 0.2 A g^{-1} , the

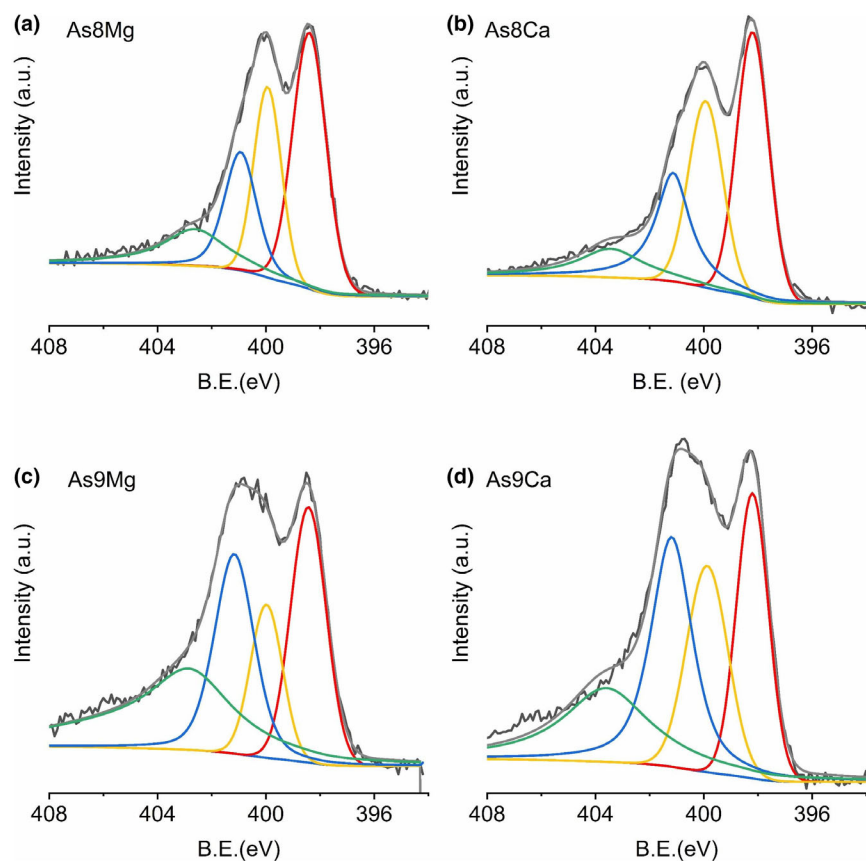


Figure 3. N1s XPS spectra of a) of As8Mg, b) As8Ca, c) As9Mg, and d) As9Ca.

reversible capacity recovers to 195 mAh g^{-1} , showing that As8Mg exhibited good rate performance and capacity reversibility even when baked at high current density. As8Ca, As9Mg, and As9Ca deliver relatively lower capacities of 154, 135, and 93 mAh g^{-1} at 0.2 A g^{-1} , respectively. Meantime, their capacity all recovers to the initial value when the current density was turned from high to low, indicating that they all have good stability and reversibility after high-rate cycling. During the first cycle, the NPCs deliver large irreversible capacities (1334 mAh g^{-1} for As8Ca, 1838 mAh g^{-1} for As8Mg, 1383 mAh g^{-1} for As9Ca), which can be ascribed to the formation of the SEI layer and irreversible sodium reaction with C-H groups.^[41] Consequently, materials with large specific surface areas suffer from low Coulombic efficiencies and it may take several cycles to achieve a stable performance. To offset the initial capacity loss on the anode side in the full energy storage configuration, where our material serves as the anode material, pre-sodiation was applied to alleviate the issues.^[42] As a result, the initial CE increases to 85% in the full SIC. In the following few cycles, the capacities of As9Mg and As9Ca stabilized, while As8Mg and As8Ca displayed significant decay, indicating structural rearrangement or reconstruction after sodiation. After the first few cycles, when the electrodes reach an “electrochemically stable structure”, As9Ca showed a negligible drop in capacity compared with As8Ca, while there is a large fall between As8Mg and As9Mg. One possible reason for the differences could be the loss of pyridinic N which has higher activity compared to other types of N,^[43–45] causing a decrease in pseudocapacitive-contributed capacity. Since the heteroatom loss from As8Mg to As9Mg (15%) is even less than that from As8Ca to

As9Ca (23%), the much higher capacity of As8Mg compared to As9Mg (Figure 4c), on the other hand, is attributed to the pseudo-graphitic nanodomains present only in As8Mg. As can be seen in Figure 1b and Figure S3b, Supporting Information, the TEM image of As8Mg shows plenty of pseudo-graphitic nanodomains, while As9Mg hardly shows ordered lattice lines. By contrast, the mesopores with graphitic marginal regions in As8Ca were well preserved after the secondary pyrolysis (As8Ca-9), as well as in As9Ca (Figure 1e and Figure S3d, Supporting Information), and these robust graphitic-layered mesopores go with a comparable capacity of As8Ca and As9Ca. Even so, As8Mg showed superior capacity performance compared to As8Ca for both pseudo-adsorption and defect adsorption, as illustrated in Figure S7, Supporting Information. Therefore, we believe the pseudo-graphitic nanodomains, play a critical role in improving the Na storage capacity and rate capability.

In addition, the storage mechanism and electrochemical kinetics of the NPCs were evaluated by CV curves at different scan rates ranging from 0.2 to 10 mV s^{-1} (Figure S8a–d, Supporting Information). As presented in Figures S8e,f, Supporting Information, the *b* values of As8Mg, As8Ca, As9Mg, and As9Ca were 0.74, 0.78, 0.68, and 0.81, respectively, suggesting a surface capacitive-dominated process with some affection from diffusion

processes for the charge storage in the four anodes (details of calculation and assignment are described in Supporting Information). The quantitative contribution of surface-controlled and diffusion-controlled processes in charge storage are shown in Figures S9a–e, Supporting Information, showing that the capacitive contributions of charge storage in As8Mg, As8Ca, As9Mg, and As9Ca were 69%, 66%, 75%, and 77% at a scan rate of 5 mV s^{-1} . As9Mg and As9Ca, which have similar heteroatoms content, demonstrated almost the same diffusion-controlled contribution percentage (25% and 23%, respectively). Meanwhile, As8Mg and As8Ca, which possess higher heteroatom contents, exhibited higher diffusion-contributed capacity, indicating that heteroatoms enhance battery-type charge storage. As the four NPCs all have a high specific surface area, it is expected that both physical capacitances generated from the electrostatic double-layer and pseudocapacitance originated from Na^+ intercalation-deintercalation and other faradic reactions take place at the near-surface. The surface-induced capacitive contribution of four electrodes all showed an upward trend, as shown in Figure S9f, Supporting Information, from around 30% to 70% as the scan rate increases from 0.2 to 5 mV s^{-1} , indicating their capacity is mainly from pseudocapacitive contribution at high rates. This upward trend is due to the diffusive capacity decay because Na ions are unable to diffuse into and leave the deeper parts of electrode material in the short time imposed by the increased scan rate.^[46]

Figure 4d showed the impedance plots of four NPCs electrodes after the CV test, all displaying a smaller semicircle at high frequency and a line at low frequency representing charge-transfer resistance (R_{ct}) and the Warburg impedance (Z_w) related to the diffusion of Na^+ in the

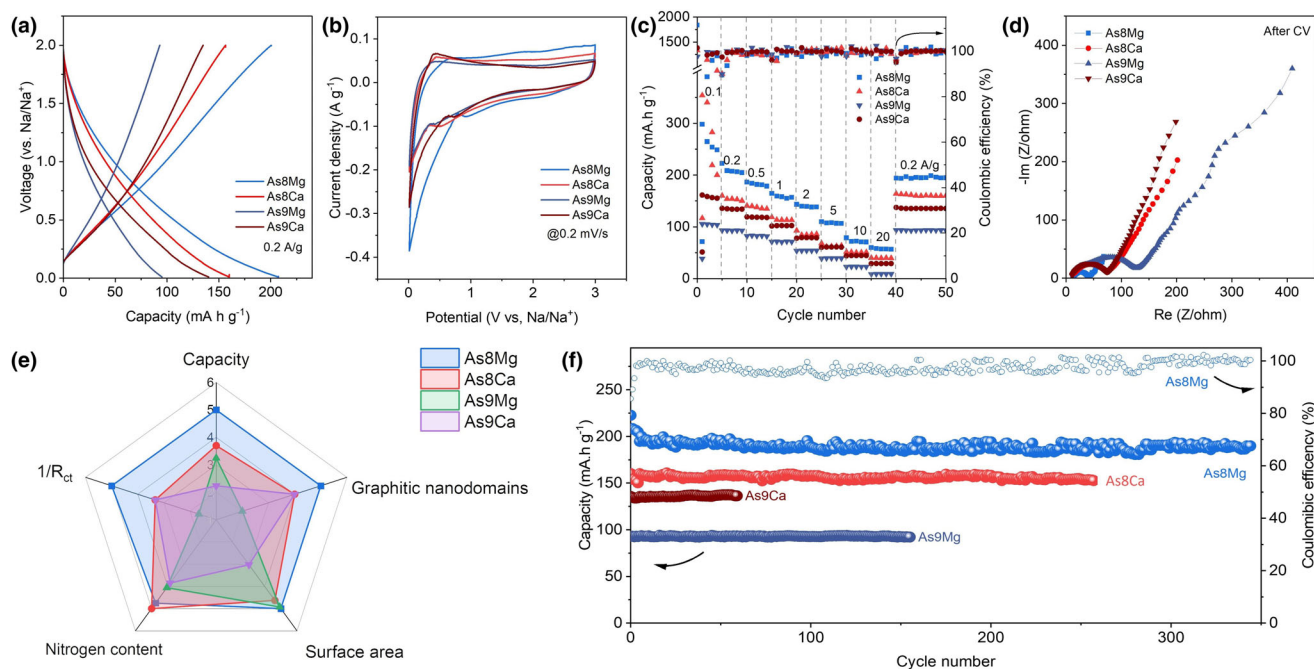


Figure 4. a) Galvanostatic charge/discharge curves at a current density of 0.2 A g^{-1} , b) CV curves, c) specific capacities and coulombic efficiency under different current densities, d) Nyquist plots of As8Mg, As8Ca, As9Mg, and As9Ca after CV test. e) Proposed index of performance and properties radar plot for four NPCs. f) Cycling performance of the samples with a current density of 0.2 A g^{-1} .

electrodes, respectively. As8Mg has the smallest semicircle ($R_{ct} = 30 \Omega$), implying the fastest charge-transfer process due to numerous pseudo-graphitic nanodomains. As8Ca and As9Ca showed similar R_{ct} values around 60Ω , while As9Mg had a much larger R_{ct} (90Ω) than As8Mg, which is attributed to the loss of pseudo-graphitic nanodomains. A pentagonal radar plot is proposed to present capacity and association with respective anode chemistries, where smaller charge-transfer resistance, nitrogen content, surface area and graphitic nanodomains were discussed. As shown in Figure 4e, the As8Mg holds the smallest R_{ct} , most favorable nanostructure, pseudo-graphitic nanodomains, and highest capacity. As mentioned before, the pseudo-graphitic nanodomains in As8Mg contribute to the high capacity, thus in the index of graphitic nanodomains, As8Mg was appointed as the highest (normalized to 5), As8Ca and As9Ca were normalized to 4, while As9Mg, which contains no graphitic nanodomains, was appointed as the lowest.

Moreover, the cycling stability of the NPCs anodes was recorded at a current density of 0.2 A g^{-1} , which started with the 50th cycle, after the first 50 cycles running for rate performance (Figure 4f). All electrodes had outstanding cycling performance, and As8Mg exhibited a retention of 98.7% with almost 100% coulombic efficiency. Based on the above results, the N-doped As8Mg with abundant pseudo-graphitic nanodomains exhibits a capacitive energy storage behavior with relatively high capacity, making it a promising anode for sodium-ion capacitors.

To show the merits of As8Mg as an anode in SIC device, activated carbon (AC) is selected as a cathode for the full cell configuration as schematically illustrated in the inset of Figure 5a. The AC cathode provides a capacity of 56 mAh g^{-1} in the potential window from 2 to 4 V (vs Na^+/Na), as shown in Figure S10, Supporting Information. First,

the As8Mg anode was first pre-sodiated to offsetting the initial irreversible capacity loss. Then, the full cell was assembled and cycled within a potential window of 0.5–4 V, and the voltage of AC cathode and As8Mg anode were recorded as shown in Figure S11, Supporting Information. The cathode/anode weight ratio is optimized as 4:1, ensuring proper utilization of the capacity on both sides. As shown in Figure 5b, the galvanostatic charge/discharge profiles of As8Mg//AC at various current densities from 0.1 to 10 A g^{-1} are similar to that of the anode material, again indicating that the storage mechanism in the SIC device is mainly pseudocapacitive. The overall cell capacitance at 0.1 A g^{-1} was as high as 153 F g^{-1} based on the mass of the As8Mg anode, and a specific capacitance of 79 F g^{-1} was obtained at 10 A g^{-1} , as shown in Figure 5c. At 0.1 A g^{-1} , the As8Mg//AC device gives an energy density of 224 Wh kg^{-1} and a power density of 53 W kg^{-1} . Even at a power density of 10.4 kW kg^{-1} , the capacitor still provides an impressive energy density of 51 Wh kg^{-1} and a cell capacitance of 40 F g^{-1} , demonstrating a promising device for high-power energy storage applications.

Figure 5d displays the Ragone plot of As8Mg//AC at different current densities and compares the values to other SIC devices based on other carbon materials and oxides. The performance of the samples is compared with 3D framework carbons from direct calcination of sodium citrate 3DFC//3DFAC,^[47] interlaced Sb_2O_3 nanosheets and Sb_2S_3 micro-nanospheres on carbon fiber cloth SO/CFC//CFs,^[48] porous networks with layer-structured V_2O_5 nanowires and carbon nanotubes AC// V_2O_5 /CNT,^[49] hierarchically porous peanut shell nanosheets (PSNC) PSNC//PSOC,^[50] ultra-thin hollow carbon nanospheres UTH-CNs/ACs,^[51] graphitic mesocarbon microbead MCMB-G//AC,^[52] and pyroprotein-derived carbon fibers PP-CF-2000// $\text{Na}_{1.5}\text{VPO}_{4.8}\text{F}_{0.7}$.^[53] Among all these porous carbon-based SICs, As8Mg//AC

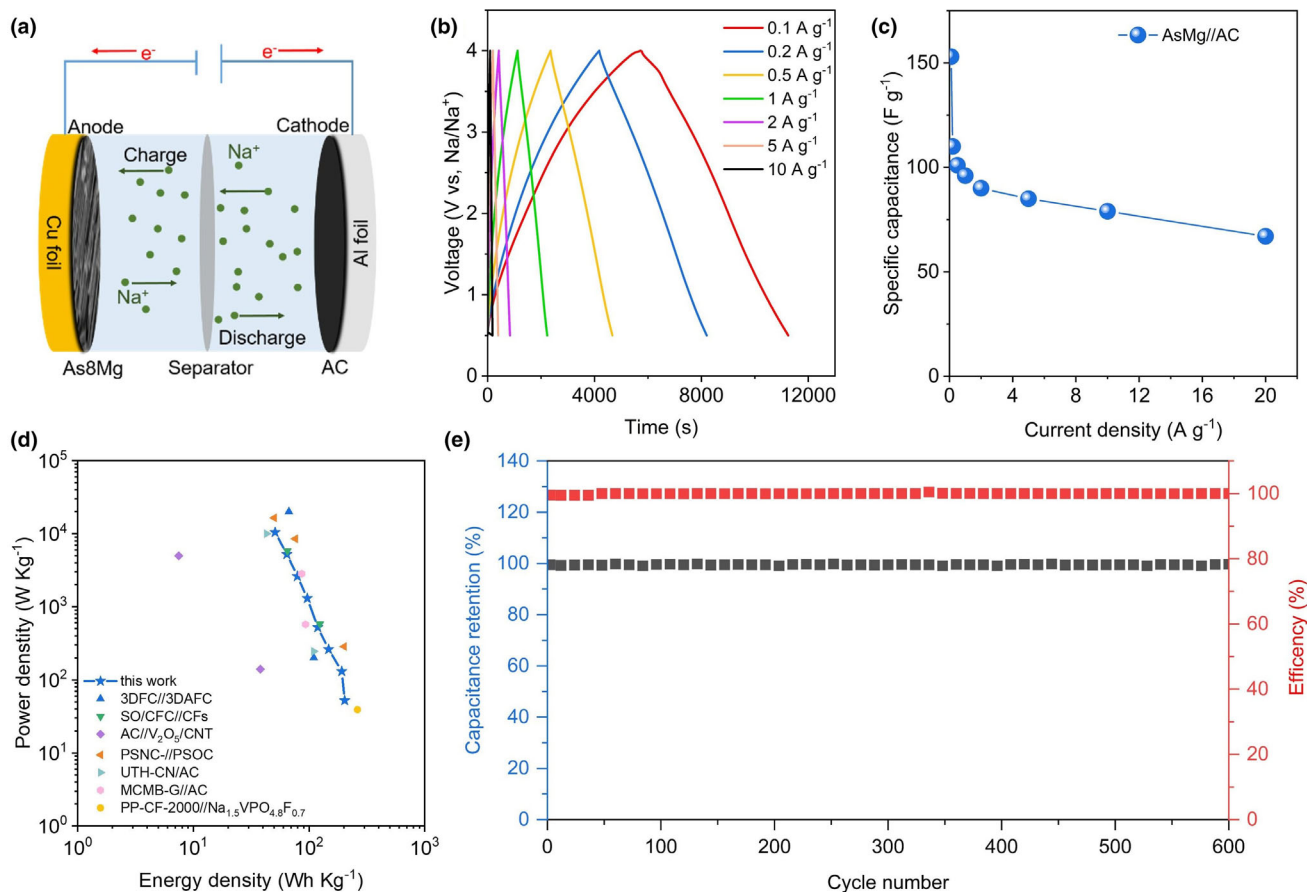


Figure 5. Electrochemical analyses of the As8Mg//AC and As8Mg//As8Mg sodium-ion hybrid capacitors in the range of 0.5–4 V. a) schematic of assembled full cell, b) galvanostatic charge/discharge profiles at different current density, and c) rate performance of As8Mg//AC SIC. d) Energy–power density performance comparison (all active mass normalized) of As8Mg//AC SIC versus state-of-the-art reported sodium-ion capacitors. e) The cycle performance of As8Mg//AC SIC over 600 charge/discharge cycles with a specific current of 0.2 A g⁻¹.

delivers a considerably high-power energy density. Moreover, it achieved 99.7% retention over 600 cycles at 0.2 A g⁻¹ with a corresponding coulombic efficiency of 99.9% (Figure 5e).

3. Conclusion

In conclusion, nitrogen-doped porous carbons with different graphitic nanodomains were made by ionothermal synthesis in MgCl₂·6H₂O and CaCl₂·2H₂O and used as anode materials in sodium-ion capacitors. As8Mg displays a high reversible capacity of 254 mAh g⁻¹ at 0.1 A g⁻¹, superb rate performance with 50 mAh g⁻¹ left at 20 A g⁻¹, and remarkable cycling stability (192 mAh g⁻¹ for 600 cycles at 0.2 A g⁻¹). The Na storage mechanism of NPCs is dominated by pseudocapacitive behavior, enabling fast charge/discharge. As such, As8Mg-based SIC achieved high-energy power densities (51 Wh kg⁻¹ @ 10–410 W kg⁻¹) with good cycling stability. We expect the templating strategy will add new and efficient features to the construction of NPCs with superior capacity performance and pseudo-graphitic nanodomains, worth getting more attention in sodium-ion capacitors.

4. Experimental Section

Materials: Adenosine was purchased from Aldrich. Magnesium chloride hexahydrate (≥99%) and calcium chloride-dihydrate (≥99%) were purchased from Carl Roth and Fisher chemical, respectively. Polyvinylidene fluoride (PVDF) and N-Methyl-2-pyrrolidone (NMP) were from Sigma Aldrich and Fisher chemical, respectively. The carbon black (Super P) conductive was obtained from Alfa Aesar. 1 M Sodium hexafluorophosphate (NaPF₆) in ethylene carbonate and diethyl carbonate (30:70, vol.%) was purchased from E-lyte Innovations GmbH. Chemicals are all used as received.

Synthesis: In a typical procedure of As8Mg synthesis, adenosine (2 g) and MgCl₂·6H₂O (20 g) were mixed by grinding in a mortar. The mixture was heat-treated at 800 °C for 2 h with a heating rate of 1 °C min⁻¹ in a nitrogen atmosphere. After cooling down, the solid was washed with hydrochloric acid (1 M, 400 mL) 3 times and water 2 times at room temperature. Then the material was dried in a 60 °C oven for 6 hours and then in a 150 °C vacuum oven overnight to remove the absorbed water. The final product was obtained with a yield of around 25%–28%. The samples were named AsNM, where As represents adenosine, the N (number) means the pyrolysis temperature (e.g., 8 for 800 °C), and M (metal) represents the metal chlorides (Mg as MgCl₂·6H₂O, Ca as CaCl₂·2H₂O).

Characterization: Powder X-ray diffraction patterns were recorded with the Rigaku SmartLab instrument with a radiation source of Cu-Kα (λ = 1.5418 Å). X-ray photoelectron spectroscopy was carried out on Thermo Scientific K-Alpha.

Inductively coupled plasma optical emission spectroscopy (ICP-OES) was performed on a PerkinElmer ICP-OES Optima. Scanning electron microscopy (SEM) and energy-dispersive X-ray (EDX) spectroscopy were recorded on a LEO 15550-Gemini Zeiss scanning electron microscope, coupled with Oxford Instruments EDX analyzer. Transmission electron microscopy images (TEM) were obtained from JEOL_F200. Nitrogen adsorption and desorption isotherms at 77 K were recorded on a Quantachrome Quadrasorb SI apparatus and Brunauer–Emmett–Teller (BET) method was used to calculate the specific surface area (S_{BET}) from nitrogen adsorption data ($P/P_0 < 0.2$).

Electrochemical measurements: The electrochemical behaviors were tested in 2016-typical half-cells. The 80 wt% active materials, 10 wt% carbon black (Super P), and 10 wt% PVDF solution (5 wt% in NMP) were mixed in NMP and stirred for 4 h to make a homogeneous slurry, then coated on the copper coil, and finally dried overnight at 60 °C under vacuum atmosphere. The coated copper coil was cut into 15 mm discs and used as working electrodes with a mass loading of around 1 mg. The cells were fabricated using Na coil (15 mm in diameter) as reference electrode and counter electrode, glass fiber as a separator, 1 M NaPF₆ in ethylene carbonate and diethyl carbonate (30:70, vol.%) as electrolyte. The galvanostatic charge/discharge measurements and cycling properties were measured at a potential range of 0.01–2 V on BioLogic's potentiostats. The capacitance of the full cell was calculated based on the total mass of anode and cathode active materials.

Acknowledgements

We gratefully appreciate Antje Völkel for measuring TGA, DSC and elemental analysis, Bolortuya Badamdorj for transmission electron microscopy measurements, and Jessica Brandt for measuring inductively coupled plasma spectroscopy. C. L. acknowledges the China Scholarship Council for financial support. We are grateful to the Max Planck Society for financial support. Open Access funding enabled and organized by Projekt DEAL.

Conflict of Interest

The authors have declared no conflict of interest.

Supporting Information

Supporting Information is available from the Wiley Online Library or from the author.

Keywords

anode, graphitic nanodomains, N-doped carbons, sodium-ion capacitor, template

Received: June 29, 2023

Revised: September 3, 2023

Published online: September 22, 2023

- [1] G. G. Amatucci, F. Badway, A. Du Pasquier, T. Zheng, *J. Electrochem. Soc.* **2001**, 148, A930.
- [2] D. P. DiVincenzo, E. J. Mele, *Phys. Rev. B* **1985**, 32, 2538.
- [3] D. A. Stevens, J. R. Dahn, *J. Electrochem. Soc.* **2001**, 148, A803.
- [4] P. Cai, K. Zou, X. Deng, B. Wang, M. Zheng, L. Li, H. Hou, G. Zou, X. Ji, *Adv. Energy Mater.* **2021**, 11, 2003804.
- [5] C. Choi, D. S. Ashby, D. M. Butts, R. H. DeBlock, Q. Wei, J. Lau, B. Dunn, *Nat. Rev. Mater.* **2020**, 5, 5.
- [6] Y. Wang, Y. Song, Y. Xia, *Chem. Soc. Rev.* **2016**, 45, 5925.
- [7] Y. Shao, M. F. El-Kady, J. Sun, Y. Li, Q. Zhang, M. Zhu, H. Wang, B. Dunn, R. B. Kaner, *Chem. Rev.* **2018**, 118, 9233.
- [8] H. Wang, D. Mitlin, J. Ding, Z. Li, K. Cui, *J. Mater. Chem. A* **2016**, 4, 5149.
- [9] S. K. Park, S. H. Kwon, S. G. Lee, M. S. Choi, D. H. Suh, P. Nakhnivej, H. Lee, H. S. Park, *ACS Energy Lett.* **2018**, 3, 724.
- [10] D. Li, C. Ye, X. Chen, S. Wang, H. Wang, *J. Power Sources* **2018**, 382, 116.
- [11] J. Ding, Z. Li, K. Cui, S. Boyer, D. Karpuzov, D. Mitlin, *Nano Energy* **2016**, 23, 129.
- [12] H.-J. Kang, Y. S. Huh, W. B. Im, Y.-S. Jun, *ACS Nano* **2019**, 13, 11935.
- [13] C.-C. Hu, K.-H. Chang, M.-C. Lin, Y.-T. Wu, *Nano Lett.* **2006**, 6, 2690.
- [14] M. Okubo, E. Hosono, J. Kim, M. Enomoto, N. Kojima, T. Kudo, H. Zhou, I. Honma, *J. Am. Chem. Soc.* **2007**, 129, 7444.
- [15] D. Choi, G. E. Blomgren, P. N. Kumta, *Adv. Mater.* **2006**, 18, 1178.
- [16] Q. Wei, R. H. DeBlock, D. M. Butts, C. Choi, B. Dunn, *Energy Environ. Mater.* **2020**, 3, 221.
- [17] J. B. Cook, H.-S. Kim, T. C. Lin, C.-H. Lai, B. Dunn, S. H. Tolbert, *Adv. Energy Mater.* **2017**, 7, 1601283.
- [18] T. Or, K. Kaliyappan, G. Li, S. Abureden, Z. Bai, Z. Chen, *Electrochim. Acta* **2020**, 342, 136024.
- [19] N. Fechner, M. Antonietti, *Nano Today* **2015**, 10, 593.
- [20] Z. Tian, Y. Zhang, J. Zhu, Q. Li, T. Liu, M. Antonietti, *Adv. Energy Mater.* **2021**, 11, 2102489.
- [21] B.-H. Hou, Y.-Y. Wang, Q.-L. Ning, W.-H. Li, X.-T. Xi, X. Yang, H.-J. Liang, X. Feng, X.-L. Wu, *Adv. Mater.* **2019**, 31, 1903125.
- [22] B. Cao, H. Liu, B. Xu, Y. Lei, X. Chen, H. Song, *J. Mater. Chem. A* **2016**, 4, 6472.
- [23] X. Yao, Y. Ke, W. Ren, X. Wang, F. Xiong, W. Yang, M. Qin, Q. Li, L. Mai, *Adv. Energy Mater.* **2019**, 9, 1803260.
- [24] J. Chmiola, G. Yushin, Y. Gogotsi, C. Portet, P. Simon, P. L. Taberna, *Science* **2006**, 313, 1760.
- [25] Z. Le, F. Liu, P. Nie, X. Li, X. Liu, Z. Bian, G. Chen, H. B. Wu, Y. Lu, *ACS Nano* **2017**, 11, 2952.
- [26] L. Zhou, K. Zhang, Z. Hu, Z. Tao, L. Mai, Y.-M. Kang, S.-L. Chou, J. Chen, *Adv. Energy Mater.* **2018**, 8, 1701415.
- [27] F. Sun, X. Liu, H. B. Wu, L. Wang, J. Gao, H. Li, Y. Lu, *Nano Lett.* **2018**, 18, 3368.
- [28] L. Xie, F. Su, L. Xie, X. Guo, Z. Wang, Q. Kong, G. Sun, A. Ahmad, X. Li, Z. Yi, C. Chen, *Mater. Chem. Front.* **2020**, 4, 2610.
- [29] L. Chen, W. Duan, B. Yang, B. Liu, H. Li, J. Lang, J. Chen, *ChemistrySelect* **2020**, 5, 5824.
- [30] R. Wang, S. Wang, X. Peng, Y. Zhang, D. Jin, P. K. Chu, L. Zhang, *ACS Appl. Mater. Interfaces* **2017**, 9, 32745.
- [31] Y.-B. Yin, J.-J. Xu, Q.-C. Liu, X.-B. Zhang, *Adv. Mater.* **2016**, 28, 7494.
- [32] J. Chen, B. Yang, H. Hou, H. Li, L. Liu, L. Zhang, X. Yan, *Adv. Energy Mater.* **2019**, 9, 1803894.
- [33] J. Pampel, A. Mehmood, M. Antonietti, T. P. Fellingner, *Mater. Horiz.* **2017**, 4, 493.
- [34] J. Pampel, Ionothermal Carbon Materials. Doctoral Thesis thesis, Universität Potsdam, Potsdam, Germany **2016**.
- [35] B. Marczevska, K. Marczewski, *Z. Phys. Chem.* **2010**, 224, 795.
- [36] G.-J. Lee, S.-I. Pyun, *Langmuir* **2006**, 22, 10659.
- [37] C. Merlet, B. Rotenberg, P. A. Madden, P.-L. Taberna, P. Simon, Y. Gogotsi, M. Salanne, *Nat. Mater.* **2012**, 11, 306.
- [38] Y. He, R. Qiao, J. Vatamanu, O. Borodin, D. Bedrov, J. Huang, B. G. Sumpter, *J. Phys. Chem. Lett.* **2016**, 7, 36.
- [39] K. Ramachandran, S. A. El-Khodary, G. Subburam, Y. Cui, S. Li, J. Li, J. Wang, X. Liu, J. Lian, H. Li, *Electrochim. Acta* **2022**, 403, 139675.
- [40] J. R. Dahn, T. Zheng, Y. Liu, J. S. Xue, *Science* **1995**, 270, 590.
- [41] Z. Wang, L. Qie, L. Yuan, W. Zhang, X. Hu, Y. Huang, *Carbon* **2013**, 55, 328.
- [42] D. Dewar, A. M. Glushenkov, *Energy Environ. Sci.* **2021**, 14, 1380.
- [43] J. Gu, Z. Du, C. Zhang, S. Yang, *Adv. Energy Mater.* **2016**, 6, 1600917.

- [44] Y. Xie, Y. Chen, L. Liu, P. Tao, M. Fan, N. Xu, X. Shen, C. Yan, *Adv. Mater.* **2017**, 29, 1702268.
- [45] H. He, D. Huang, Y. Tang, Q. Wang, X. Ji, H. Wang, Z. Guo, *Nano Energy* **2019**, 57, 728.
- [46] X. Pu, D. Zhao, C. Fu, Z. Chen, S. Cao, C. Wang, Y. Cao, *Angew. Chem. Int. Ed.* **2021**, 60, 21310.
- [47] B. Yang, J. Chen, S. Lei, R. Guo, H. Li, S. Shi, X. Yan, *Adv. Energy Mater.* **2018**, 8, 1702409.
- [48] S. Liu, Z. Cai, J. Zhou, M. Zhu, A. Pan, S. Liang, *J. Mater. Chem. A* **2017**, 5, 9169.
- [49] Z. Chen, V. Augustyn, X. Jia, Q. Xiao, B. Dunn, Y. Lu, *ACS Nano* **2012**, 6, 4319.
- [50] J. Ding, H. Wang, Z. Li, K. Cui, D. Karpuzov, X. Tan, A. Kohandehghan, D. Mitlin, *Energ. Environ. Sci.* **2015**, 8, 941.
- [51] Y. S. Yun, S. Y. Cho, H. Kim, H.-J. Jin, K. Kang, *ChemElectroChem* **2015**, 2, 359.
- [52] P. Han, X. Han, J. Yao, L. Zhang, X. Cao, C. Huang, G. Cui, *J. Power Sources* **2015**, 297, 457.
- [53] J. Choi, M. E. Lee, S. Lee, H.-J. Jin, Y. S. Yun, *ACS Appl. Energy Mater.* **2019**, 2, 1185.